RSC Applied Interfaces

ROYAL SOCIETY OF CHEMISTRY

PAPER

View Article Online
View Journal | View Issue

Cite this: *RSC Appl. Interfaces*, 2025, **2**, 472

Mitigating polysulfide crossover in lithium–sulfur batteries with polymer-coated separators†

R. Blake Nuwayhid,[a] Junghoon Yeom,[b] Hunter O. Ford,[a] Zachary G. Neale,[c] Michael W. Swift,[d] Noam Bernstein,[d] Rachel E. Carter[c] and Jeffrey W. Long *[c]

Lithium–sulfur (Li–S) batteries promise high energy density and sustainability advantages by using earth-abundant sulfur as a key component, yet practical performance is limited by the complexity of sulfur-based redox reactions. One key challenge is the dissolution and redistribution of soluble lithium polysulfide (LiPS) intermediates from the sulfur cathode, which leads to irreversible loss of active material, poor cycle life, and high self-discharge rates. To ameliorate this issue, we use initiated chemical vapor deposition (iCVD) to conformally coat conventional polyolefin separators with an ultrathin (40–400 nm) copolymer, poly(divinylbenzene-*co*-(dimethylaminomethyl)styrene). This pDVB-*co*-DMAMS copolymer is designed with amine functionalities to interact with LiPSs and mitigate cathode-to-anode crossover, while DVB comonomer units serve as cross-linkers that improve mechanical integrity. We evaluate the electrochemical properties of prototype Li–S cells that include pDVB-*co*-DMAMS-coated separators and sulfur-infused carbon nanofoam paper cathodes. Separators with the thickest pDVB-*co*-DMAMS coating (400 nm) provide extended protection against self-discharge, while 40 nm pDVB-*co*-DMAMS coatings enable the highest overall rate capability and cycling stability while still maintaining reasonably low self-discharge rates. Post-cycling analysis of anode, separator, and cathode components, in conjunction with computational efforts, confirms that pDVB-*co*-DMAMS delays LiPSs crossover through chemical adsorption in the polymer-coated separator. The pDVB-*co*-DMAMS-coated separators also interact with Li metal anode to form favorable chemical speciation at the solid-electrolyte interphase that stabilizes the Li surface for Li–S cell operation.

Received 30th October 2024,
Accepted 16th December 2024

DOI: 10.1039/d4lf00369a

rsc.li/RSCApplInter

Introduction

Lithium–sulfur (Li–S) batteries are emerging as a promising energy-storage alternative to conventional lithium-ion batteries (LIBs) by offering the advantages of an earth-abundant cathode material (sulfur) that also exhibits high specific capacity (1675 mA h g^{-1} theoretical). Pairing sulfur-based cathodes with Li metal anodes yields a materials-level theoretical specific energy of ~2500 W h kg^{-1}.[1–3] Practical packaged Li–S cells typically achieve ~400 W h kg^{-1},[4] with energy content varying with such factors as cathode thickness and sulfur loading. Because elemental sulfur is a poor electron conductor, Li–S cathodes must be constructed to include appreciable amounts of conductive carbon. Advanced porous carbons have been designed as sulfur hosts to further optimize mass, volume, and areal capacity values for sulfur-based cathodes.[3,5,6]

The high specific capacity of sulfur-based electrodes arises from the conversion reaction between elemental sulfur and lithium sulfide ($S_8 + 16Li^+ + 16e^- \leftrightarrow 8\ Li_2S$), which proceeds through a complex pathway involving multiple soluble polysulfides. These intermediate lithium polysulfides (LiPSs), including Li_2S_8, Li_2S_6, and Li_2S_4, unavoidably dissolve in the electrolyte during cycling, leading to active material loss at the cathode. Such polysulfide species may also cross over to the Li anode where they are chemically reduced, then diffuse back to the cathode to be re-oxidized in a process described as the polysulfide shuttle effect.[7,8] The combination of these polysulfide-based processes results in rapid capacity fade and high self-discharge rates during the operation of Li–S batteries, limiting the practical application of this otherwise promising energy-storage technology.

Several materials strategies have been used to address the problems imposed by these polysulfide shuttle effects,

[a] *National Research Council Postdoctoral Associate, U.S. Naval Research Laboratory, Washington, DC, USA*
[b] *Multifunctional Materials Branch (Code 6350), U.S. Naval Research Laboratory, Washington, DC, USA*
[c] *Surface Chemistry Branch (Code 6170), U.S. Naval Research Laboratory, Washington, DC, USA. E-mail: jeffrey.w.long26.civ@us.navy.mil*
[d] *Center for Materials Physics and Technology (Code 6390), U.S. Naval Research Laboratory, Washington, DC, USA*

† Electronic supplementary information (ESI) available. See DOI: https://doi.org/10.1039/d4lf00369a

including: (*i*) physical confinement or chemical interaction of LiPSs within the sulfur-containing cathode; (*ii*) optimization of electrolyte composition to reduce LiPSs solubility or using solid-state electrolytes; (*iii*) physical shielding or chemical trapping effects at the separator through functional coatings; and (*iv*) artificial protection layers at the Li anode to inhibit chemical reactions of polysulfide with Li metal; and (*v*) using catalysts to accelerate the redox kinetics of LiPSs.[8–10] For example, conventional porous polyethylene/polypropylene separators can be coated with chemical functionalities that induce adsorption, repulsion, or entrapment of LiPSs, thereby acting as a barrier to crossover of dissolved LiPSs from the cathode to the Li anode.[11,12] Additional benefits of functionalized separators include enhancing thermal stability, Li^+ conductivity, electrolyte wettability, sulfur utilization, rate capability, and specific capacity.[13–15] Such coatings should be kept thin and conformal to avoid occluding the pores of the separator (as small as 100 nm) and introducing unnecessary resistance and additional mass/volume to the cell.[11,16] Atomic layer deposition (ALD) is a popular thin-film coating technique that has been successfully used to modify various battery components, but ALD coatings (typically rigid inorganic materials) require elevated temperatures for growth that are near the decomposition temperature of common polyethylene/polypropylene separators (130–150 °C).[17,18]

Alternatively, initiated chemical vapor deposition (iCVD) can be used to generate ultrathin polymer coatings at mild substrate temperatures (20–50 °C) to modify thermally sensitive materials.[19–21] Polymers with varying functionality can be generated by iCVD, typically using vinyl-substituted monomers that have some degree of volatility. Because iCVD is a non-line-of-sight deposition technique, it is amenable to coating complex 3D substrates,[22–24] as would be the case for porous battery separators. Recent studies have demonstrated that iCVD-modified separators can enhance Li–S and Li-ion cell performance.[25,26] This deposition technique has also been shown to operate in large-scale roll-to-roll coating systems,[27–29] which should be compatible with existing battery manufacturing processes.

We use iCVD to conformally coat porous polyethylene (PE) battery separators with the copolymer, poly(divinylbenzene-*co*-(dimethylaminomethyl)styrene) (pDVB-*co*-DMAMS), which is designed to express multiple characteristics that are beneficial to Li–S cell operation. The DMAMS subunit provides an amine functionality to interact with LiPSs and to stabilize the Li metal anode interface, while the DVB subunit crosslinks the copolymer to prevent its dissolution/delamination into the battery electrolyte. We assess the impact of these (pDVB-*co*-DMAMS)-coated separators on electrochemical performance in Li–S coin cells that also include freestanding carbon nanofoam paper (CNFP) cathodes[30] with high sulfur loading (3 mg cm^{-2}) and Li foil anodes, ascertaining such critical metrics as self-discharge rate and charge–discharge cycling stability. Based on post-cycling analysis using a suite of characterization techniques and computation by atomistic modelling, we elucidate the interactions between pDVB-*co*-DMAMS with LiPSs that lessen

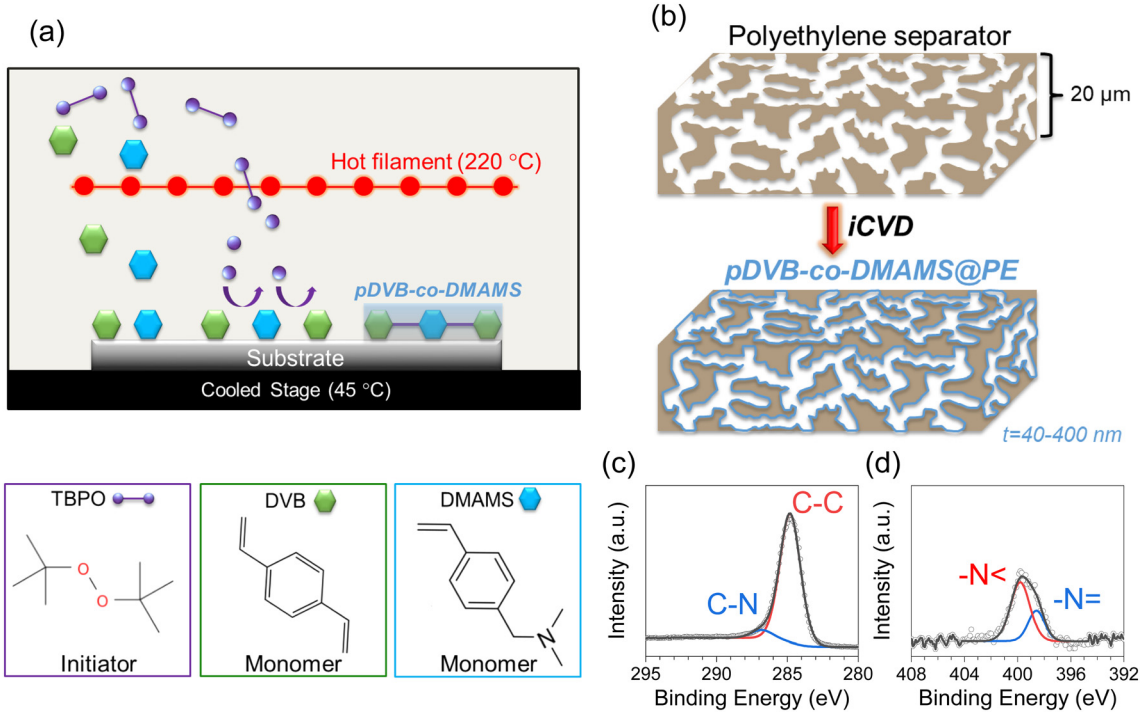

Fig. 1 (a) Schematic of iCVD-based synthesis of pDVB-*co*-DMAMS and chemical structures of initiator and monomers used. (b) Schematic of ideal iCVD deposition to form conformal polymer coatings on porous separators. Core-level (c) C 1s and (d) N 1s XPS spectra of iCVD-generated pDVB-*co*-DMAMS deposited on planar Si substrates.

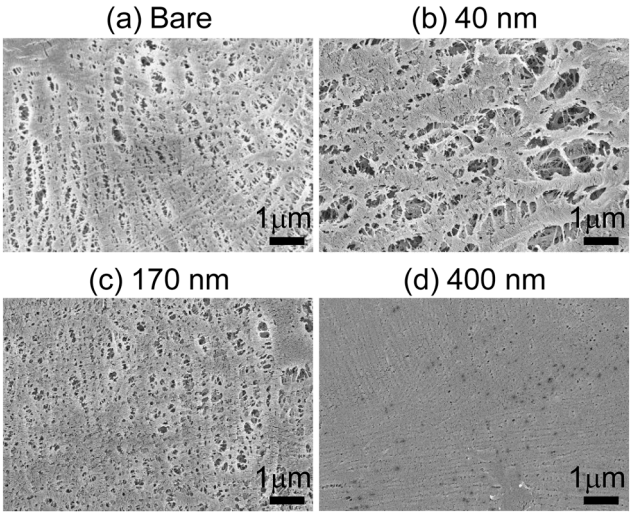

Fig. 2 Scanning electron micrographs of (a) bare polyethylene and (b–d) 40 nm-, 170 nm-, and 400 nm-iCVD@PE separators, showing the topside relative to the orientation of the separator in the iCVD reactor.

cathode-to-anode crossover and improve Li–S cycling performance.

Results and discussion

Poly(DVB-*co*-DMAMS) synthesis and electrochemical properties

The iCVD process for generating the copolymer, pDVB-*co*-DMAMS, is depicted in Fig. 1a, where DVB and DMAMS monomer vapors are introduced into the vacuum chamber along with the *tert*-butyl peroxide (TBPO), a common initiator used with iCVD. The heated filament located above the temperature-controlled stage decomposes TBPO to form radicals that initiate the polymerization of DVB and DMAMS monomers adsorbed on the surfaces of the PE separators. Under optimized conditions, the polymer conformally coats all surfaces throughout the separator volume (Fig. 1b). The chemical composition of pDVB-*co*-DMAMS is assessed *via* XPS of films deposited on Si substrates (Fig. 1c and d). The C 1s core-level spectra show two peaks at 284.8 eV and 286.1 eV, assigned to C–C and C–N bonding, respectively. The N 1s core-level spectra show two peaks: –N < at 399.8 eV and –N = at 398.6 eV. The –N < peak accounts for ~70% of the N 1s peak intensity, qualitatively similar to results recently reported for iCVD-generated pDMAMS.[23] Quantification of the XPS peaks yields a C:N atomic ratio of 19.9 (with negligible oxygen, 1 at%) that corresponds to a 1 : 1.1 ratio of DVB : DMAMS, demonstrating the ability of iCVD to deposit high-purity pDVB-*co*-DMAMS films.

Copolymer coating thickness is controlled by exposure time to monomers and initiator in the iCVD chamber. Thickness values of ~40 nm, 170 nm, and 400 nm for 25, 50, and 90 min depositions, respectively, are measured based on spectroscopic ellipsometry analysis of planar Si chips that are included in the iCVD chamber along with the porous separators (Fig. S1†). The porosity of pDVB-*co*-DMAMS-coated PE separators, hereby referred to as "iCVD@PE" for simplicity, are examined using scanning electron microscopy (SEM). Fig. 2 displays SEM images of the separators after deposition at the boundary facing up towards the deposition chamber ceiling and filaments, and those at the boundary resting on the chamber floor are shown in Fig. S2.† The inherent porosity is largely maintained for the 40 nm-iCVD@PE separator (Fig. 2b), while pore diameter diminishes significantly with 170 nm-iCVD@PE and 400 nm-iCVD@PE separators (Fig. 2c and d). Qualitatively similar trends are noted in micrographs taken on the back side of the separator (Fig. S2†), confirming that iCVD polymer generation is generally conformal and uniform through the separator thickness.

The ionic transport properties of pDVB-*co*-DMAMS-coated PE separators are examined by electrochemical impedance spectroscopy (EIS) in symmetric cells with stainless-steel (SS) ion-blocking electrodes, which ensure that all measured ionic contributions are from the electrolyte-soaked separator. For all electrochemical experiments, we use an electrolyte comprising

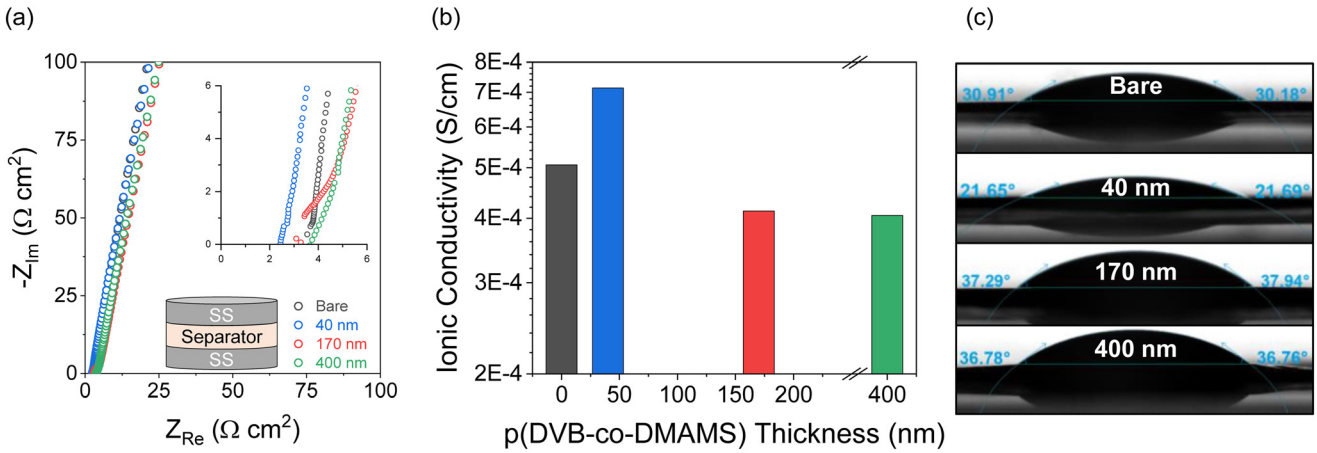

Fig. 3 (a) Nyquist plots from EIS measurements with stainless-steel symmetric cells containing bare or iCVD@PE separators. (b) Ionic conductivities extracted from Nyquist plots. (c) Contact-angle measurements of bare and iCVD@PE separators wetted with a droplet of the Li–S battery electrolyte (1 M LiTFSI + 0.2 M $LiNO_3$ in DOL/DME).

1 M LiTFSI + 0.2 M $LiNO_3$ in DOL/DME, a commonly used composition for Li–S cell testing (see further discussion below). Nyquist plots for all cells show continuous increase in the imaginary impedance as frequency decreases, consistent with double-layer formation on the blocking electrodes (Fig. 3a). The high-frequency real impedance for all cells ranges between 2 and 5 Ω cm^2; values taken from the intercept with the real-impedance axis are used to calculate the ionic conductivity of the electrolyte-infused separator, according to the equation, $\sigma_i = \frac{L}{R \times A}$, where L is the separator thickness (20.4 μm), R is the total resistance, and A is the area of the electrode (see values in Fig. 3b). Ionic conductivity is higher with the 40 nm-iCVD@PE separator (0.71 mS cm^{-1}) *versus* the bare separator (0.51 mS cm^{-1}), which we attribute to improved wetting of the PE-based separator with the polar liquid electrolyte (1 M LiTFSI + 0.2 M $LiNO_3$ in DOL/DME), as shown by decreasing contact angle with an electrolyte droplet (Fig. 3c). Thicker iCVD@PE coatings (≥170 nm) decrease conductivity modestly as the pores of the polyethylene separator become more occluded and the electrolyte contact angle increases.

Poly(DVB-*co*-DMAMS) in lithium–sulfur batteries

Cycling performance. We first assess the voltage stability of pDVB-*co*-DMAMS in Li–Cu cell configurations containing coated separators, confirming a wide stability window ranging from Li plating potentials (−0.05 V) to oxidative conditions (up to 3 V) beyond the typical upper limit for Li–S cells (Fig. S3†). The performance of iCVD@PE separators in Li–S cells also containing S-infused carbon nanofoam paper (S@CNFP) cathodes[30] is initially evaluated with galvanostatic cycling and EIS analysis. When cycling at a typical rate of 0.1 A g_{sulfur}^{-1}, all cells exhibit the two-plateau discharge profile commonly reported for Li–S chemistry, with an initial step at ~2.4 V for conversion of S_8 to Li_2S_4 followed by further reduction to insoluble Li_2S at ~2.1 V (Fig. 4a). The average discharge voltage is ~50 mV higher for cells with iCVD@PE separators.

On the reverse charge step, Li_2S is oxidized back to S_8, which is represented by a single broad plateau at ~2.35 V for all cells. At the early stage of the charging process, there is an "overpotential" to oxidize the insoluble and insulating Li_2S back to soluble LiPSs, which manifests as an initial peak above the charging plateau (Fig. 4a, inset).[31] This charging peak (~24 mV above the plateau) is most pronounced in the Li–S cell with the bare separator, whereas it is essentially zero for the 40 nm-iCVD@PE and minimal (~4 mV) for 170 nm-iCVD@PE and 400 nm-iCVD@PE. The decrease in this initial charge voltage confirms that Li_2S oxidation within the CNFP is more kinetically facile in such cases.

The charge–discharge voltage hysteresis is also lower in all cells with pDVB-*co*-DMAMS coatings compared to those with the bare separator, and lowest overall for 40 nm-iCVD@PE. This trend is further supported by EIS analysis of Li–S cells before cycling (Fig. S4†), which shows minimal difference in cell impedance with the bare separator *versus* the 40 nm-iCVD@PE separator. Alternatively, 170–400 nm@PE cells show a 1.5× higher impedance due to the thicker polymer film and less free volume within the separator for liquid electrolyte.

Long-term Li–S cell cycling behavior is assessed by first applying 5 formation cycles at 0.1 A g_{sulfur}^{-1} followed by 100 cycles at 0.2 A g_{sulfur}^{-1}. All cells show similar first-cycle capacity (~900–980 mA h g_{sulfur}^{-1}) at 0.1 A g_{sulfur}^{-1}, but measured capacities diverge after a few cycles (Fig. 4b). Cells with the 40 nm-iCVD@PE separator exhibit the best capacity retention, maintaining ~640 mA h g_{sulfur}^{-1} after 105 cycles compared to ~530 mA h g_{sulfur}^{-1} for all other cells, while also showing better cell-to-cell consistency than each of the other cell types (Fig. S5†). Voltage profiles for cycles 5, 25, 50, and 100 at 0.2 A g_{sulfur}^{-1} show a high overpotential on initial charge for all cells except with the 40 nm-iCVD@PE (Fig. S6†). The 40 nm-iCVD@PE cell displays a steady discharge plateau throughout 105 cycles indicative of facile reduction of $S_8 \rightarrow Li_2S$, while each of the other cells show broad features at the $Li_2S_{6(l)} \rightarrow Li_2S_{4(l)}$ and $Li_2S_{2(s)} \rightarrow Li_2S_{(s)}$ transitions. These features arise due to the resistive nature of the thicker pDVB-*co*-DMAMS coatings. Increasing voltage polarization is further supported by EIS measurements after cycling (Fig. 4c), where the 40 nm-iCVD@PE cell shows a single semicircular feature of ~5 Ω cm^2 diameter compared to multiple semicircles of ~20 Ω cm^2 magnitude for 170 nm- and 400 nm-iCVD@PE cells. We also note that the series resistance increases linearly with pDVB-*co*-DMAMS coating thickness, consistent with a decrease in free volume for electrolyte in the separator.

The rate performance of cells with bare and iCVD@PE separators is displayed in Fig. 4d. All cells with iCVD@PE separators deliver higher capacity than the bare separator at rates of 0.1 and 0.2 A g_{sulfur}^{-1}, with the 40 nm-iCVD@PE separator showing the highest overall capacity retention. Cells with thicker pDVB-*co*-DMAMS coatings show decreasing capacity at rates of 0.5–2 A g_{sulfur}^{-1}, but the 40 nm-iCVD@PE cell exhibits a 1.3× higher capacity than the bare cell at 0.5 A g_{sulfur}^{-1}. Upon returning to 0.1 A g_{sulfur}^{-1}, the 40 nm-iCVD@PE cell exhibits the best overall capacity retention, providing 87.5% of its cycle-10 capacity at cycle 40 after the high-rate excursion. We attribute the improved rate performance of the 40 nm-iCVD@PE cell to a thinner pDVB-*co*-DMAMS coating that preserves the porous transport pathways of the separator while still stabilizing the electrode/electrolyte interfaces. At the other end of the pDVB-*co*-DMAMS thickness range, the 400 nm-iCVD@PE cell exhibits a higher capacity at 0.1–0.2 A g_{sulfur}^{-1} than the 170 nm-iCVD@PE coating. This trend is supported by the decreased resistivity in Li/Li cells with the 400 nm-iCVD@PE separator (Fig. S7†), suggesting that rate capability may also be impacted by differences in the solid-electrolyte interphase (SEI) at the Li metal anode. The overall cycling performance benefits of the iCVD@PE separators are summarized in Table 1 and are compared to their self-discharge performance.

Self-discharge behavior. We assessed the ability of iCVD@PE separators to mitigate polysulfide shuttling effects

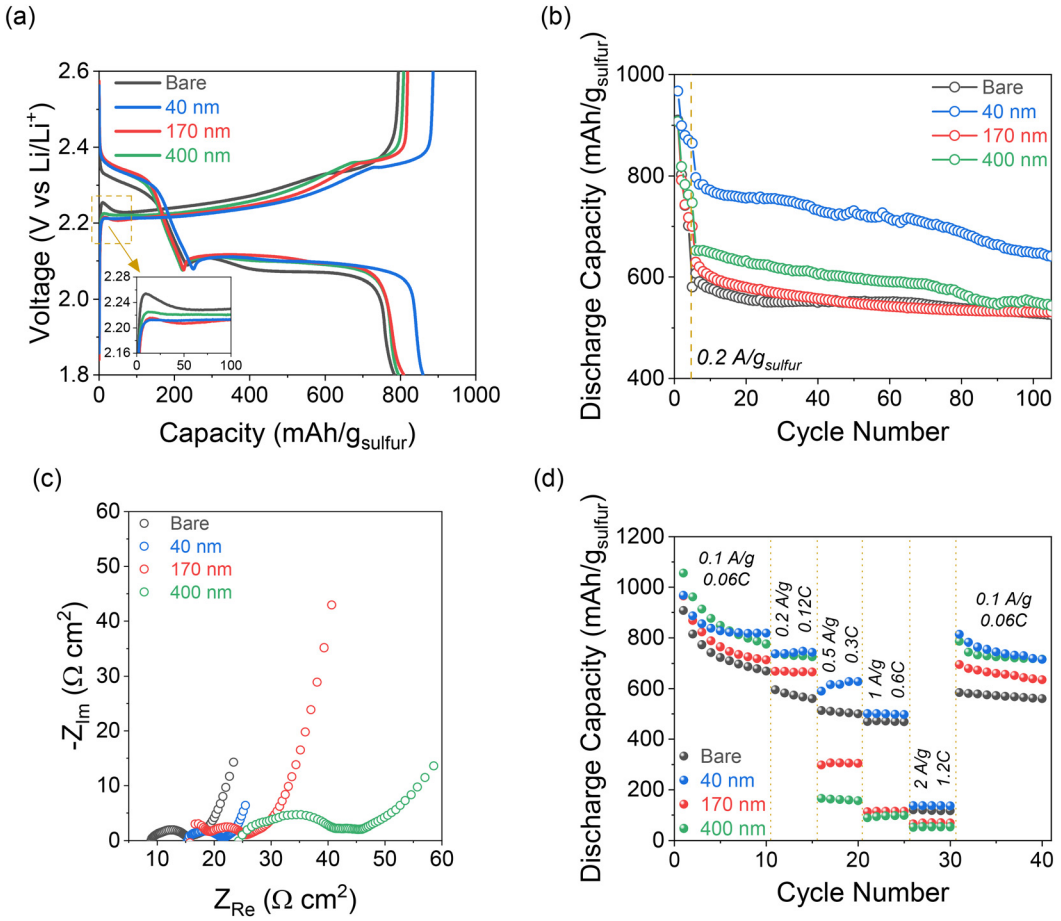

Fig. 4 (a) Galvanostatic charge–discharge curves for Li–S cells with bare and iCVD@PE separators. Inset shows overpotential for Li_2S oxidation at the beginning of the charge half-cycle. (b) Capacity retention for the average of two cells of each type cycled at 0.1 A g_{sulfur}^{-1} for 5 cycles followed by 100 cycles at 0.2 A g_{sulfur}^{-1}. (c) Nyquist plots from EIS measurements of Li–S cells after completing 105 cycles. (d) Rate performance under galvanostatic control with imposed currents from 0.1–2 A g_{sulfur}^{-1}.

Table 1 Li–S electrochemical performance summary of iCVD@PE separators

Separator	Ionic conductivity[a] (S cm^{-1})	Capacity at 0.5 A g_{sulfur}^{-1}[b] (mA h g_{sulfur}^{-1})	Capacity after 100 cycles[c] (mA h g_{sulfur}^{-1})	Self-discharge rate[d] (mV day^{-1})
Bare	5.06×10^{-4}	500	532	35.7
40 nm-iCVD@PE	7.14×10^{-4}	627	641	18.6
170 nm-iCVD@PE	4.13×10^{-4}	304	532	12.9
400 nm-iCVD@PE	4.05×10^{-4}	156	544	10.0

[a] Ionic conductivity of the electrolyte-soaked separator determined by EIS measurements in Fig. 3a. [b] Capacity of Li–S cells the fifth cycle at 0.5 A g_{sulfur}^{-1} from the rate test in Fig. 4d. [c] Capacity of Li–S cells after 100 cycles at 0.2 A g_{sulfur}^{-1} in Fig. 4b. [d] Self-discharge rate from Fig. 6d.

by visually and spectroscopically tracking crossover of Li_2S_8 through various separators using an H-cell glassware configuration, with a Li_2S_8-containing electrolyte on one side of the separator and the native electrolyte on the other (Fig. 5a–d). The bare separator allows Li_2S_8 crossover almost immediately, as evidenced by appearance of a dark brown solution on the opposite side of that separator after 1 h. In contrast, H-cells with iCVD@PE separators show solution breakthrough of a light-yellow hue, with intensity diminishing for thicker pDVB-*co*-DMAMS coatings. This qualitative trend is maintained for 24 h of solution crossover, with the cell containing bare separator turning dark red on the opposing side *versus* light brown with the iCVD@PE separators. Analysis of recovered solutions by UV–visible spectroscopy further confirms the trend of decreasing intensity in Li_2S_8 solution crossover with increasing pDVB-*co*-DMAMS coating thickness on the PE separator (Fig. 5e).

Self-discharge behavior is assessed in Li–S cells that were initially subjected to 14 charge–discharge cycles ending in a final charge half-cycle, followed by monitoring open-circuit

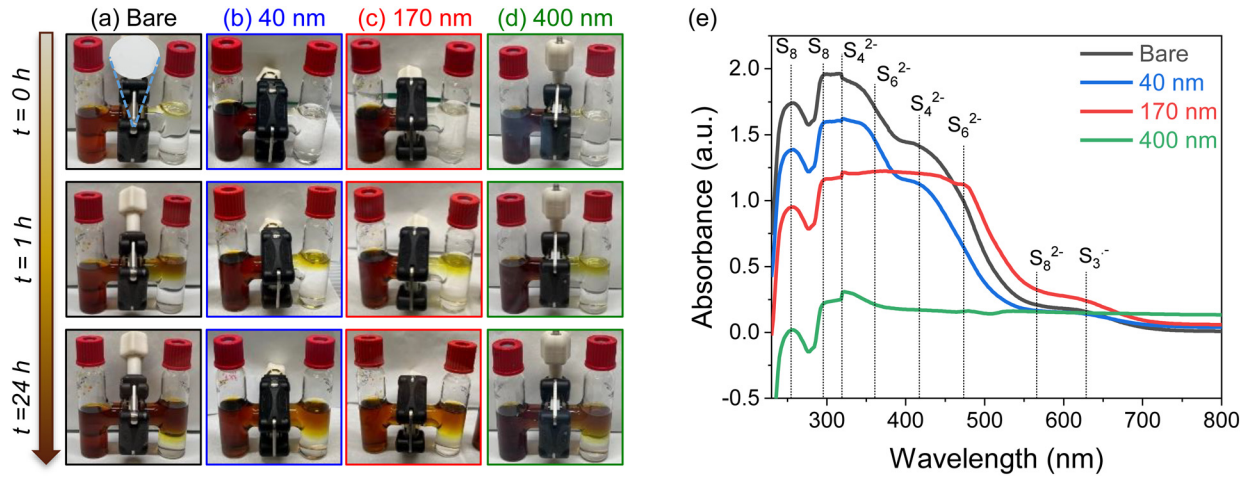

Fig. 5 Images of H-cell diffusion crossover tests at 0, 1, and 24 hours for (a) bare, (b) 40 nm-, (c) 170 nm-, and (d) 400 nm-iCVD@PE separators. In the initial state, the left-side compartment contains 2 mM of Li_2S_8 in the 1 M LiTFSI + 0.2 M $LiNO_3$ in DOL:DME electrolyte and the right-side compartment contains electrolyte only. The PE separator is placed between the glass compartments, which are held together with an O-ring and spring-loaded clamp. (e) UV–vis spectra of solutions taken from the right side compartment of the H-cell after permeation through the respective separators for 24 h.

voltage (OCV) over a period of 7 days (Fig. 6b). After ~2 days, the OCV of the bare-separator cell begins to decrease substantially from 2.35 V down to 2.13 V. Cells with iCVD@PE separators exhibit significantly slower self-discharge, with the delay of voltage decay increasing with thicker pDVB-*co*-DMAMS coatings. This effect also manifests in the deliverable cell capacity following the self-discharge 7 d rest period. As depicted in Fig. 6c–f, separators with thicker pDVB-*co*-DMAMS coatings support higher post-rest discharge capacity. On the following charge step, there is some irreversible loss of capacity in cells with ≤170 nm coatings, while the cell with the 400 nm-iCVD@PE separator is able to regain 100% of its initial (pre-rest) charge capacity, consistent with its ability to best inhibit LiPS crossover. In a prior study of iCVD-generated polyimidazole coatings on battery separators, Lim *et al.*[26] reported 83.2% capacity retention for Li–S cells (using conventional carbon–sulfur powder composite cathodes) following a 12 h rest period. We performed similar tests (12 h rest; Fig. S8†) and observed 96% capacity retention for the bare separator and 100% retention with each of the iCVD@PE separators. This high capacity retention (low self-discharge) for all of our cells at these short 12 h rest periods is also attributable to enhanced sulfur confinement within the 3D CNFP cathodes,[30] which enables even cells with the conventional separator to remain OCV-stable for at least 48 h of rest time.

To further isolate the effect of the pDVB-*co*-DMAMS coating on LiPS crossover, we also perform similar self-discharge measurements on Li–S cells assembled without $LiNO_3$ in the electrolyte. Lithium–sulfur cells commonly include $LiNO_3$ as an electrolyte additive to mitigate undesirable reactions at the Li anode when soluble LiPSs are present.[32–35] Our results with $LiNO_3$-free cells also show that iCVD@PE separators still delay cell self-discharge (Fig. S9a†), and also improve capacity and coulombic efficiency under galvanostatic cycling (Fig. S9b†). In all cases, we observe a decrease in coulombic efficiency and faster self-discharge for cells without the $LiNO_3$ additive. Thus, the combination of both separator coating and electrolyte additive yields optimal performance for Li–S cell operation.

Post-cycling characterization of Li–S cell components

Li metal anode characterization. To further elucidate the role of the iCVD@PE separators in enhancing electrochemical performance, we disassemble Li–S cells of each type after 20 charge–discharge cycles at 0.1 A g_{sulfur}^{-1} (cycling data in Fig. S10†) and analyze the individual cell components. The separator-facing surfaces of the Li metal anodes are examined for changes in surface morphology, SEI composition, and the impact of LiPS crossover and reaction. Lithium anodes from cells cycled with a bare separator exhibit a surface morphology consisting of rough grains with voids at the grain boundaries (Fig. 7a), whereas a smoother Li metal morphology is noted from cells using the 40 nm-iCVD@PE separator (Fig. 7b). The Li anode with the 170 nm-iCVD@PE separator exhibits a rougher surface than for the 40 nm-iCVD@PE separator, with some cracking also observed (Fig. 7c). For the 400 nm-iCVD@PE, this cracking behavior exacerbated, leading to peeling of a thick film from the surface (Fig. 7d). Despite the cracking at the surface of the Li in cells cycled with 170-iCVD@PE and 400 nm-iCVD@PE separators, the larger-scale Li morphology is relatively smooth compared to Li cycled with a bare separator. In contrast, rough Li morphology is commonly reported for cycled Li–S cells due to reaction of the Li anode with dissolved LiPSs.[36–38]

X-ray photoelectron spectroscopy analysis of the Li surface provides chemical information for products formed during Li–S cell operation. We observe a lower total content of S at the Li

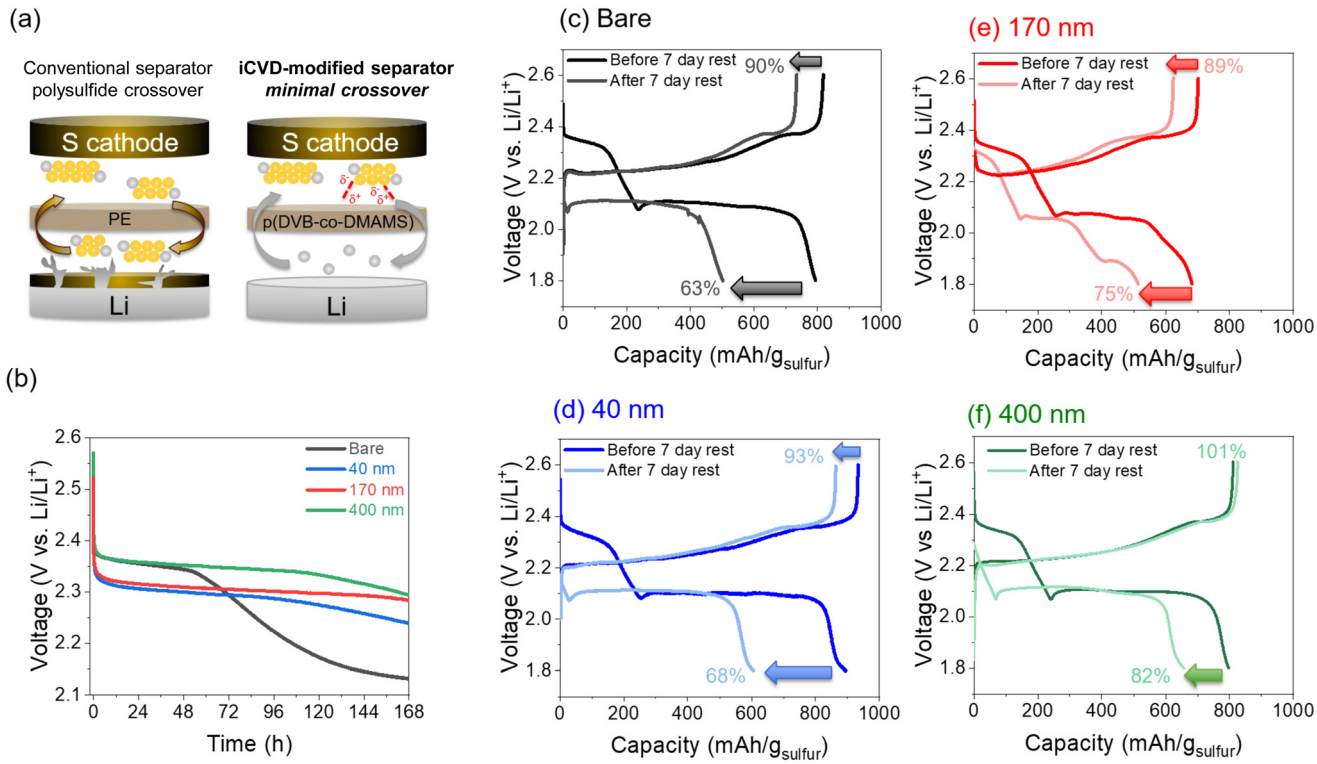

Fig. 6 (a) Schematic of the polysulfide crossover effect in conventional Li–S cells and with the iCVD@PE separator. (b) Open-circuit Li–S cell voltage recorded during a 7 d rest period. (c–f) Galvanostatic charge–discharge profiles of Li–S cells before and after the 7 d rest period with bare, 40 nm-, 170 nm-, and 400 nm-iCVD@PE separators, respectively.

surface for anodes used with all of the iCVD@PE separators, with ~1 at% S for each such case compared to 4.3 at% with the bare separator; argon-ion depth-profiling also confirms consistent chemical composition throughout the surface layer (Fig. S11†). Deconvolution of the S 2p spectra reveals additional information about S speciation (Fig. 6e). After cycling with the bare separator, the Li anode surface expresses several S species: Li_2S at 161.8 eV; terminal LiPS (S_T) or Li_2S_2 at 163.2 eV; bridging LiPS (S_B) at 164.7 eV; SO_3^{2-} at 167.7 eV; and SO_4^{2-}/R-SO_2-R at 169.3 eV (j = 3/2 binding energies).[33,38,39] Cells cycled with iCVD@PE separators display a significantly different S speciation at the Li surface. In the reduced S species region (160–166 eV), there are no peaks associated with S_B bonds but only S_T bonds, indicating that no higher order Li_2S_n (n = 4, 6, 8) are present at the Li electrode surface. Peaks for Li_2S, which can arise from the chemical reaction of LiPS with Li, are observed with iCVD@PE separators but at a lower relative intensity compared to results with the bare separator. In the oxidized sulfur species region (167–173 eV), peaks associated with SO_3^{2-} and SO_4^{2-}/R-SO_2-R are minimized at the Li metal surface for cells cycled with iCVD@PE separators. In contrast, Li cycled with the bare separator shows prominent peaks for lithium sulfates and sulfites, as would commonly occur due to the reaction of crossover LiPS with Li metal in the presence of $LiNO_3$ and LiTFSI.[37,38] Reaction of the Li metal anode with LiPS also manifests with the reduction of $LiNO_3$ to $LiNO_2$. Such reduced NO_2 species are not observed in the N 1s spectra (Fig. 7f) of the Li metal surface cycled with the iCVD@PE separators, but only the bare separator. These findings support the supposition that pDVB-*co*-DMAMS plays a role in preventing detrimental LiPS interaction with the Li metal surface.

The N 1s and F 1s spectra (Fig. 7f and g) show that the 400 nm-iCVD@PE separator produces a significantly different chemical composition at the Li anode surface, exhibiting the most N and C content, and the least amount of S and F (as quantified in Fig. S11†). We posit that the thick pDVB-*co*-DMAMS coating contacting the Li metal surface reacts to form a pDVB-*co*-DMAMS-derived passivating layer, evidenced by excess Li_3N and C–N peaks in the N 1s spectra (Fig. 7f). This supposition is further supported by our SEM observation of a thick film on the Li surface for cells cycled with the 400 nm-iCVD@PE separator (Fig. 6d), and the lower impedance measured with this separator in Li/Li symmetric cells compared to cells with the bare separator (Fig. S7†). The F 1s spectra confirms the superior SEI quality at Li from the 40 nm–iCVD@PE cell (Fig. 7g); in such case the F content is 88% LiF, which is known as a desirable SEI product.[40–42] Alternatively, the bare separator results in a F surface chemistry dominated by C–F functionalities arising from electrolyte decomposition (see also C 1s spectra in Fig. S12†) with only 21% of F content as LiF. The Li electrode from the 400 nm-iCVD@PE cell exhibits minimal F content, further evidence of its passivation from electrolyte decomposition. In combination, the XPS and SEM results confirm that the pDVB-*co*-DMAMS coating plays a significant role in mitigating LiPS crossover, and promoting favorable Li metal morphology and SEI chemistry.

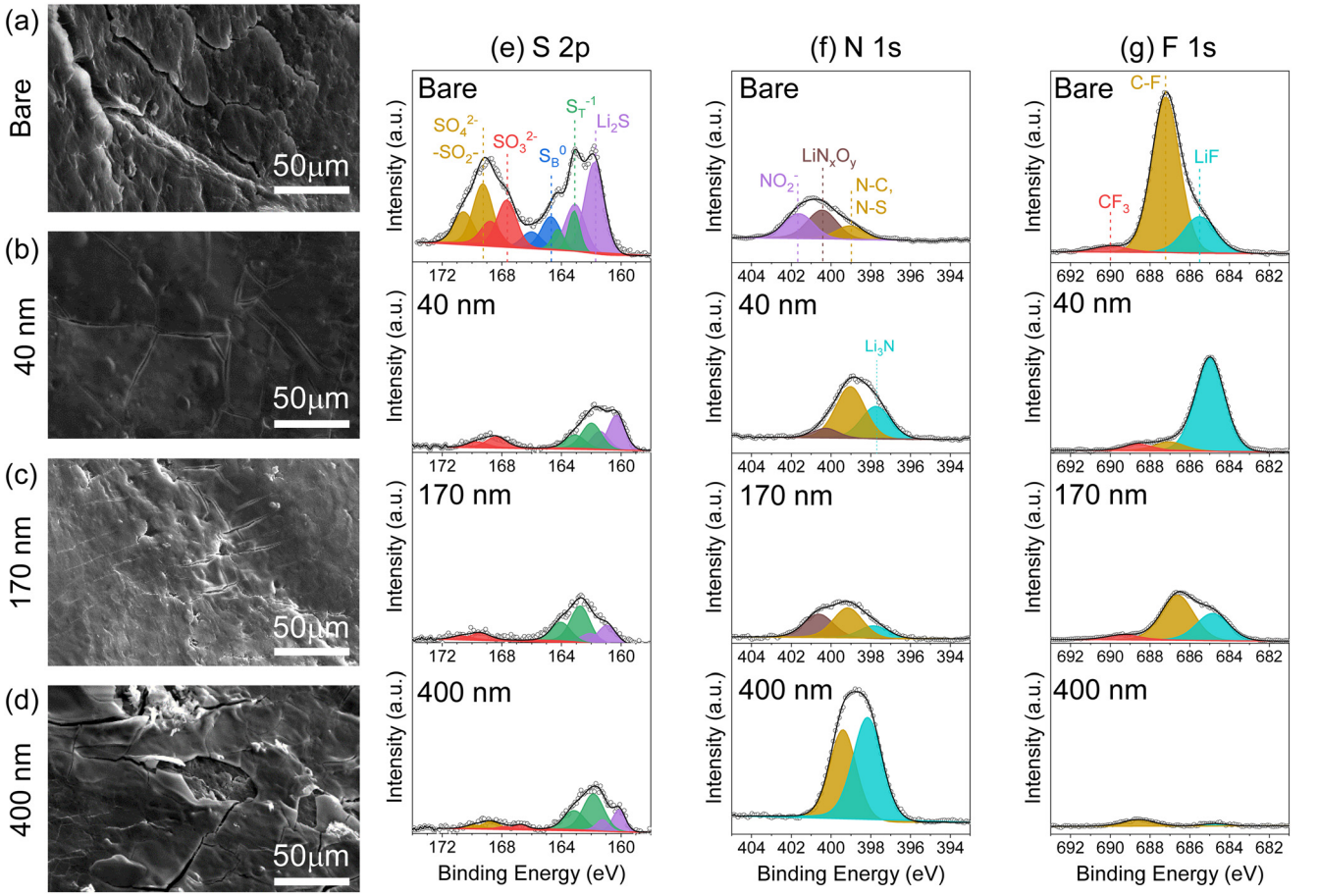

Fig. 7 Scanning electron micrographs (collected at a 45° tilt angle) for Li metal from cycled cells with (a) bare, (b) 40 nm-, (c) 170 nm- and (d) 400 nm-iCVD@PE separators. Core-level X-ray photoelectron spectra at the surface of Li metal anodes from cycled cells recorded in the (e) S 2p, (f) N 1s, and (g) F 1s regions.

Separator characterization. Separators from Li–S cells disassembled after 20 cycles are analyzed by optical imaging and SEM to determine their interaction with LiPSs, electrolyte, and other cell components (Fig. 8a–d). The bare separator (Fig. 8a) shows a significant amount of debris covering the cathode-facing surface, consistent with formation SEI/decomposition byproducts at the Li anode, as noted in Fig. 7. Elemental mapping by energy-dispersive spectroscopy (EDS) also shows that the large debris particles are S-rich (Fig. S13†). The iCVD@PE separators generally show a smoother surface morphology and less debris (Fig. 8b–d), while the 40 nm-iCVD@PE separator shows the lowest distribution of S-containing particles. The 170 nm-iCVD@PE and 400 nm-iCVD@PE separators exhibit a thick, cracked film, suggesting volume expansion and contraction with these thicker pDVB-*co*-DMAMS coatings (Fig. 8c and d), in agreement with the thick film and cracking noted on the surface of the contacting Li metal anodes (Fig. 7c and d). The inset optical images show that the separators display a darker amber color with thicker pDVB-*co*-DMAMS coatings, which is consistent with additional adsorption of LiPSs species.

These LiPS-stained separators were further extracted with DME solvent and the resulting solution characterized with UV–visible spectroscopy (Fig. 8e). The observed peaks are consistent with reduced LiPS species in LiTFSI/ether solutions, as reported in literature.[43–45] The spectra in Fig. 8e show an increase in absorbance of S_8 species for extracts of thicker pDVB-*co*-DMAMS coatings, indicating that pDVB-*co*-DMAMS is chemically trapping LiPSs[46–48] and delaying their crossover towards the Li anode.

Atomistic simulations are performed to determine the thermodynamics of the interaction between DMAMS and LiPSs. The results of these simulations indicate that Li_2S_n molecules can reversibly attach to DMAMS units in the pDVB-*co*-DMAMS layer through the nitrogen lone pair on the pedant dimethylamine group (Fig. 8f). The binding energy (calculated in vacuum using DFT) is 0.93 eV, consistent with reversible binding of LiPSs. In contrast, the bonding of LiPSs to the CNFP cathode surface (as approximated computationally by a graphene monolayer) is substantially weaker, averaging 0.48 eV in vacuum. The bonding of LiPSs with DMAMS is primarily a Lewis-base interaction between the amine and the Li^+,[49] whereas interaction with carbon surfaces is primarily driven by van der Waals forces. This large vacuum binding energy is consistent with reversible attachment of LiPSs to the pDVB-*co*-DMAMS layer in solution,

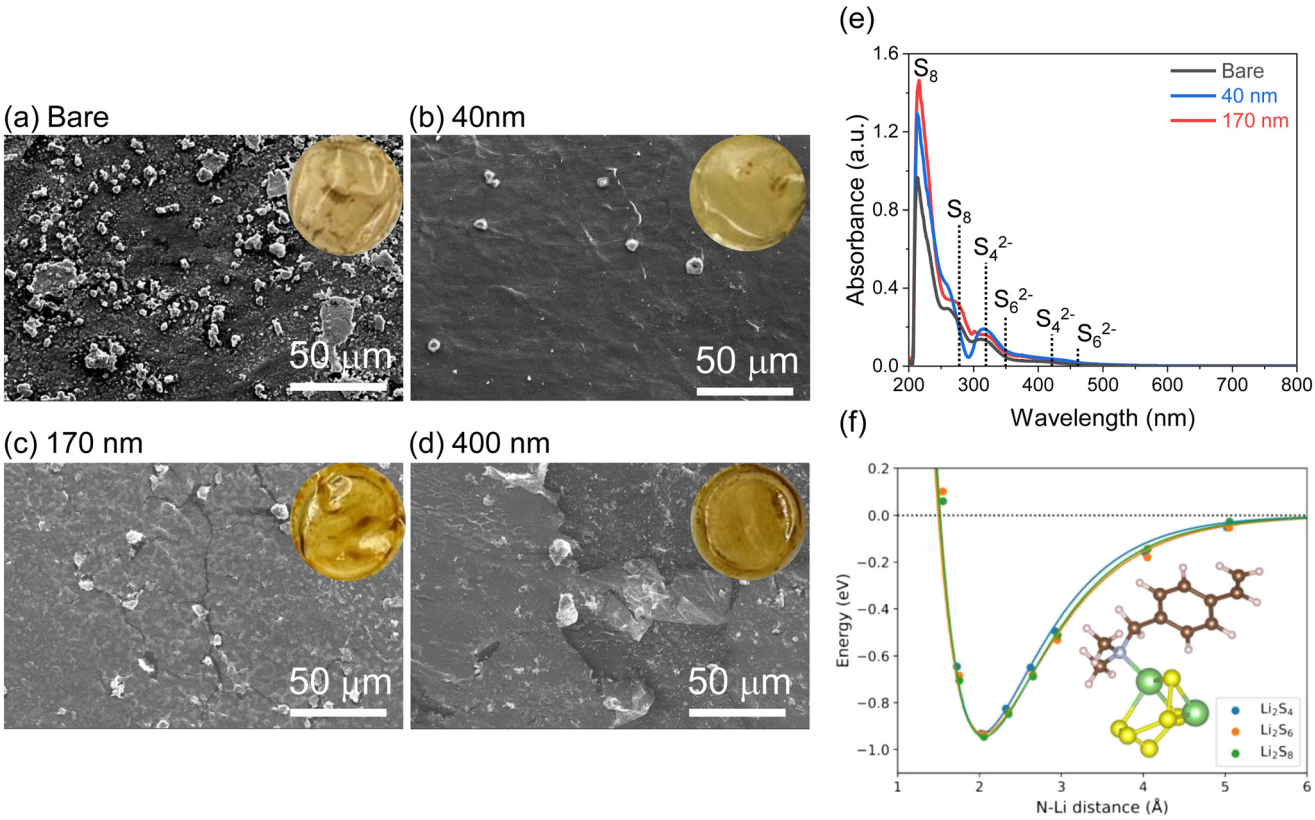

Fig. 8 (a–d) Scanning electron micrographs of bare, 40 nm-, 170 nm-, and 400 nm-iCVD@PEseparators after 20 charge–discharge cycles. Inset: optical images of recovered separators. (e) UV–vis spectra of solutions used to extract the respective harvested separators. (f) Binding energy of Li_2S_n to a DMAMS monomer, plotted as a function of N–Li distance. Points represent DFT data, and lines are fits to a Morse potential. Inset: visualization of the bonded DMAMS monomer and Li_2S_6 molecule (H shown in gray, C in brown, N in blue, Li in green, and S in yellow).

because solvation acts to weaken the bond. The reversible binding of LiPSs is crucial for maintaining a long-lasting Li–S battery, whereas if the binding forces are too strong, some sulfur-based material will be lost from the cathode.

To further explore solvation effects, we perform molecular dynamics (MD) simulations of Li_2S_6 and DMAMS in the presence of a realistic solvent (DOL : DME 1 : 1 by weight). Simulations are performed using a machine-learning interatomic potential fine-tuned based on DFT data of solvated DMAMS and LiPSs.[50,51] The binding enthalpy in the presence of solvent is 0.146 ± 0.038 eV, likely large enough to trap the polysulfide but small enough that the polysulfide is still available for further reduction during discharge. The atomistic simulations also suggest that the Li_2S_n species do not dissociate into $2Li^+ + S_n^{2-}$ in solution, but rather remain as an ion complex. Further details of the MD simulations may be found in the ESI.†

Cathode characterization. The S@CNFP cathodes cycled in Li–S cells with bare and 40 nm-iCVD@PE separators display S-rich deposits filling some cracks in the CNFP (see SEM-EDS images in Fig. S14†). The S deposits in the CNFP cracks are denser for the bare-separator cell than the 40 nm-iCVD@PE cell. Alternatively, the S@CNFP cathodes cycled with 170 nm- and 400 nm-iCVD@PE separators exhibit a surface morphology closely resembling that of the pristine CNFPs without cycling (Fig. S15†), and show no S deposits in the CNFP openings but rather a uniform distribution (Fig. S14†). The cross-sectional SEM images of each S@CNFP cathode confirm this trend, as with the bare and 40 nm-iCVD@PE cells the cathodes show a dense accumulation of particles throughout (Fig. 8e and f), while the 170 nm- and 400 nm-iCVD@PE cell cathodes show a more open structure and the gaps are unfilled. This finding is attributed to the thicker pDVB-*co*-DMAMS layer anchoring S-based species near the separator, as confirmed in Fig. 7. In the case of thin iCVD@PE coatings, we observe partial trapping of LiPSs in the S@CNFP cathode, although Fig. 7e shows additional LiPSs absorbed in the 40 nm-iCVD@PE separator *versus* with the bare separator. Furthermore, DFT calculations confirm that the binding energy of LiPSs with carbon are less than half of that for the iCVD polymer, as noted above. While the CNFP cathode architecture provides some containment and mitigation of LiPSs on its own, electrochemical performance is further enhanced by combining the S@CNFP cathode with iCVD@PE separators in Li–S cells.

Conclusions

Our findings demonstrate the efficacy of iCVD as a route to modify commercial battery separators with thin, conformal

coatings of a specifically designed copolymer—pDVB-*co*-DMAMS—that effectively mitigates the negative effects of LiPS shuttling on Li–S cell operation. In addition to reversibly adsorbing LiPSs at amine functionalities, the pDVB-*co*-DMAMS coating also interacts with the Li metal anode surface to form a stabilizing layer, while also improving the wettability of the PE separator to liquid electrolyte. As a result, Li–S cells that include these iCVD@PE separators exhibit enhanced electrochemical performance in terms of resilience to self-discharge, better charge–discharge cycle life, and greater capacity retention with increasing discharge rate. Specifically, thicker coatings of 400 nm-iCVD@PE offer extended protection towards self-discharge, while 40 nm-iCVD@PE separators provide the best overall electrochemical performance while maintaining effective self-discharge mitigation. Combining these polysulfide-mitigating, iCVD-modified separators with advanced carbon cathode architectures such as the CNFP opens new possibilities for Li–S battery performance and application.

Experimental

Initiated chemical vapor deposition of polymer coatings

A GVD Corporation "iLab" reactor was used to iCVD-synthesize pDVB-*co*-DMAMS. In a typical deposition, the 4-DMAMS monomer (synthesized according to our previous report[23]) was heated to 70 °C, the DVB monomer independently heated to 50 °C, and the di-*tert*-butyl peroxide (TBPO 98%, Aldrich) initiator was maintained at room temperature, all in separate source vessels. The lines from source vessels to the reactor were heated to 80 °C in order to minimize vapor condensation. The DVB flow was controlled through a ball-valve while DMAMS and TBPO flow to the reactor were controlled using mass-flow controllers set for rates of 2.1 SCCM DMAMS and 1 SCCM TBPO, respectively. The reactor substrate stage was maintained at 45 °C and a pressure of ~200 mTorr was maintained in the deposition chamber using an automated throttle valve. The initiator was thermally activated by resistively heating a Nichrome filament to ~220 °C (35 V, ~2A applied) mounted above the substrate stage. Depositions were conducted directly on Entek Gold LP separators (UHMWPE, 19.4 μm thick, 37% porosity) and on Si chips that were subsequently used for thickness measurements. Ellipsometry measurements on these Si chips were collected at variable angles (55°, 65°, 75°) and film thickness was modeled using a general oscillator model consisting of Tauc–Lorentz and Gaussian oscillators (J. A. Woolam M-2000 spectroscopic ellipsometer). The bare and pDVB-*co*-DMAMS-coated separators were dried at 60 °C under vacuum overnight, then quickly transferred to an Ar-filled glovebox (<0.1 ppm H_2O, O_2) to minimize moisture exposure.

Sulfur-CNFP cathode synthesis

The CNFPs were synthesized as previously reported.[30,52] Sized (15 mm diameter) and weighed pieces of CNFP were supported on a stainless-steel mesh placed above a bed of 1 g sulfur powder inside a PTFE chamber. Vapor infiltration with sulfur was achieved by heating the chamber inside a muffle furnace for 4 hours at 175 °C, as previously described.[53–55] After infiltration, the chamber was removed from the oven and cooled for 30 min; the CNFPs were then removed from the chamber, weighed, and immediately transferred to an Ar glovebox. The resulting S@CNFP cathodes contained an average of 38.4% sulfur by weight, corresponding to ~3 mg cm^{-2} areal S loading.

Electrochemistry

Lithium–sulfur cells were constructed inside an Ar-filled glovebox using CR2032 coin-cell hardware (Hoshen Corp.) with a 9/16″ diameter Li anode (99.9% MSE supplies, 0.6 mm thick), ¾″ diameter Entek separator with 70 μL of 1 M lithium bis(trifluoromethanesulfonyl)imide (LiTFSI)/0.2 M lithium nitrate ($LiNO_3$) in 1,3-dioxolane (DOL)/1,2-dimethoxyethane (DME) electrolyte, and a 15 mm diameter S@CNFP cathode. The Li/Li symmetric cells, SS/SS symmetric cells, and Li/Cu cells were assembled in a similar fashion. All electrochemical cycling was performed inside environmental chambers at 25 °C with control and data collection provided by a Maccor Model 4300 test system; an Ametek Parstat multichannel potentiostat with PMC-1000 modules was used for EIS and cycling. All cells were cycled at specified rates normalized to the mass of sulfur (A g_{suflur}^{-1}), and operated with voltage limits of 1.8 and 2.6 V. Impedance measurements were performed by scanning the frequency between 600 kHz–0.06 Hz with a sinusoidal amplitude of 10 mV for cells in an OCV state.

Characterization

Diffusion-crossover tests. An H-type glass cell was assembled with the respective separator placed between the two chambers, with 2 mM Li_2S_8 in the Li–S battery electrolyte on one side and native electrolyte on the other (10 mL each). Photographs of the cells were taken over intervals of time. This test was performed in the Ar-filled glovebox due to the sensitivity of the LiPS solutions to O_2, which induces color changes.

UV–visible spectroscopy. UV–visible spectroscopy was performed using a Perkin Elmer Lambda 1050+ instrument. The crossover solution from the H-cell tests was measured directly. Recovered separators from cycled cells were placed in a vial with 2 mL of DME and soaked for 24 h, from which 0.1 mL diluted in a quartz cuvette with 2.9 mL DME (to bring solution absorbance within a suitable range for the spectrometer). The cuvettes were sealed inside the Ar-filled glovebox and analyzed immediately to minimize effects from air exposure.

X-ray photoelectron spectroscopy. Lithium metal electrodes were retrieved from cycled coin-cells and each rinsed with 0.5 mL of acetonitrile to remove salt residue, followed by drying under vacuum. Lithium metal electrodes were assembled in a vacuum-transfer vessel inside the glovebox, pumped down in the glovebox antechamber to create the inert vacuum seal, and transferred to the XPS load lock to minimize exposure of the Li

metal to air. X-ray photoelectron spectra were collected with monochromatic Al Kα radiation (12 kV) at an anode current of 6 mA (Nexsa Surface Analysis System, ThermoFisher). The flood gun was used for charge neutralization with all XPS scans. Survey spectra were collected using a pass energy of 200 eV and a binding energy step size of 1 eV. High-resolution spectra were collected using a pass energy of 20 eV and a binding energy step size of 0.1 eV. Monatomic Ar^+ depth profiling was performed at an ion energy of 2 keV and a calibrated sputter rate of 7.8 nm min^{-1} of Ta_2O_5. Data analysis was performed with Thermo Avantage® software using 70/30 Gaussian/Lorentzian pseudo-Voigt functions with Shirley backgrounds. High-resolution peak area ratios were used for elemental quantification, using tabulated Thermo relative sensitivity factors and all peaks were calibrated to the C–C peak at 284.8 eV.

Scanning electron microscopy. Lithium anodes and CNFP cathodes were cleaned as described above before mounting on sample stubs in the glovebox and sealing in an air-tight container for quick transfer to the SEM (~10 s air exposure). The separators were air-exposed to deposit a thin-layer of Au prior to SEM imaging in order to minimize charging effects. Scanning electron microscopy was performed on a Thermo Fisher Scientific Quattro Environmental SEM with the e-beam voltage of 15 kV. X-ray energy dispersive spectroscopy (EDS) maps were taken using an EDAX Octane Elite detector.

Atomistic simulations. First-principles calculations were performed using the Vienna *Ab Initio* Simulation Package (VASP)[56] with projector-augmented wave (PAW) pseudopotentials[57] and the HSE06 range-separated hybrid functional.[58] The plane-wave energy cutoff was 500 eV and Gamma-only *k*-point sampling was used. van der Waals (vdW) interactions were included using the DFT-D3 method of Grimme with zero-damping,[59] with HSE06-fitted parameters s_8 = 0.109 and $s_{r,6}$ = 1.129. Calculations of solvation effects were based on a MACE interatomic potential.[51] The potential was fine-tuned starting from the MACE-MP-0 foundation model[50] using a dataset of DFT energies, forces, and stresses of 2836 atomic configurations with an average of ~200 atoms each. The fine-tuning procedure achieved low root-mean-square errors (RMSE) compared to a reserved test set: 1.5 meV per atom in energies and 48.2 meV $Å^{-1}$ in forces. Additional information on the atomistic modelling is described in the ESI.†

Data availability

Data generated and analyzed in this study are included in the article and its ESI.†

Author contributions

R. B. N. and H. O. F. conceived the research idea and performed the iCVD depositions. R. B. N. performed electrochemical tests and spectroscopic characterizations. J. Y. and H. O. F. performed SEM analysis. Z. G. N. synthesized the CNFPs. M. W. S. and N. B. performed the atomistic simulations. J. W. L. and R. E. C. directed and guided the research project. R. B. N. wrote the manuscript with input from all authors.

Conflicts of interest

The authors have no conflicts to declare.

Acknowledgements

Financial support for this research was provided by the U.S. Office of Naval Research under award numbers N0001424WX00013 and N0001424WX00370. R. B. N. and H. O. F. are National Research Council Postdoctoral Associates at the U.S. Naval Research Laboratory.

References

1 Z. W. Seh, Y. Sun, Q. Zhang and Y. Cui, *Chem. Soc. Rev.*, 2016, **45**, 5605–5634.
2 A. Manthiram, Y. Fu, S. H. Chung, C. Zu and Y. S. Su, *Chem. Rev.*, 2014, **114**, 11751–11787.
3 Y. Yang, G. Zheng and Y. Cui, *Chem. Soc. Rev.*, 2013, **42**, 3018–3032.
4 G. Zhou, H. Chen and Y. Cui, *Nat. Energy*, 2022, **7**, 312–319.
5 A. Eftekhari and D.-W. Kim, *J. Mater. Chem. A*, 2017, **5**, 17734–17776.
6 M. A. Pope and I. A. Aksay, *Adv. Energy Mater.*, 2015, **5**, 1500124.
7 Q. Pang, X. Liang, C. Y. Kwok and L. F. Nazar, *Nat. Energy*, 2016, **1**, 16132.
8 Z. Han, S. Li, Y. Wu, C. Yu, S. Cheng and J. Xie, *J. Mater. Chem. A*, 2021, **9**, 24215–24240.
9 Y. Huang, L. Lin, C. Zhang, L. Liu, Y. Li, Z. Qiao, J. Lin, Q. Wei, L. Wang, Q. Xie and D. L. Peng, *Adv. Sci.*, 2022, **9**, e2106004.
10 G. Liu, C. Yuan, P. Zeng, C. Cheng, T. Yan, K. Dai, J. Mao and L. Zhang, *J. Energy Chem.*, 2022, **67**, 73–81.
11 L. Fan, M. Li, X. Li, W. Xiao, Z. Chen and J. Lu, *Joule*, 2019, **3**, 361–386.
12 M. Waqas, Y. Niu, M. Tang, Y. Pang, S. Ali, Y. Dong, W. Lv and W. He, *Energy Storage Mater.*, 2024, 103682, DOI: 10.1016/j.ensm.2024.103682.
13 A. Kim, S. H. Oh, A. Adhikari, B. R. Sathe, S. Kumar and R. Patel, *J. Mater. Chem. A*, 2023, **11**, 7833–7866.
14 M. Zhang, X. Zhang, S. Liu, W. Hou, Y. Lu, L. Hou, Y. Luo, Y. Liu and C. Yuan, *ChemSusChem*, 2024, **17**, e202400538.
15 X. Dong, W. Gu, X. Tong, G. Liu, J. Sun, H. Li, X. Gu, T. Zhu and S. Zhang, *Small*, 2024, **20**, 2311471.
16 J. Jang, J. Oh, H. Jeong, W. Kang and C. Jo, *Materials*, 2020, **13**, 4625.
17 S. M. George, *Chem. Rev.*, 2010, **110**, 111–131.
18 L. Ma, R. B. Nuwayhid, T. P. Wu, Y. Lei, K. Amine and J. Lu, *Adv. Mater. Interfaces*, 2016, **3**, 1600564.
19 W. E. Tenhaeff and K. K. Gleason, *Adv. Funct. Mater.*, 2008, **18**, 979–992.
20 K. K. Gleason, *Nat. Rev. Phys.*, 2020, **2**, 347–364.

21 K. K. Gleason, *Adv. Mater.*, 2024, **36**, e2306665.
22 H. Sojoudi, S. Kim, H. Zhao, R. K. Annavarapu, D. Mariappan, A. J. Hart, G. H. McKinley and K. K. Gleason, *ACS Appl. Mater. Interfaces*, 2017, **9**, 43287–43299.
23 H. O. Ford, B. L. Chaloux, B. Jugdersuren, X. Liu, C. A. Klug, J. B. Miller, X. Zuo, M. W. Swift, M. D. Johannes, J. W. Long, D. R. Rolison and M. B. Sassin, *RSC Appl. Interfaces*, 2024, **1**, 531–543.
24 M. B. Sassin, J. W. Long, J. M. Wallace and D. R. Rolison, *Mater. Horiz.*, 2015, **2**, 502–508.
25 Y. Yoo, B. G. Kim, K. Pak, S. J. Han, H. S. Song, J. W. Choi and S. G. Im, *ACS Appl. Mater. Interfaces*, 2015, **7**, 18849–18855.
26 W.-G. Lim, S. Oh, J. Jeong, W. Jang, K. I. Shim, S. Kim, J. W. Han, S. G. Im and J. Lee, *ACS Appl. Energy Mater.*, 2021, **4**, 611–622.
27 H. Şakalak, K. Yılmaz, M. Gürsoy and M. Karaman, *Chem. Eng. Sci.*, 2020, **215**, 115466.
28 C. Cheng and M. Gupta, *Ind. Eng. Chem. Res.*, 2018, **57**, 11675–11680.
29 M. Gupta and K. K. Gleason, *Thin Solid Films*, 2006, **515**, 1579–1584.
30 Z. G. Neale, M. J. Lefler, J. W. Long, D. R. Rolison, M. B. Sassin and R. Carter, *Nanoscale*, 2023, **15**, 16924–16932.
31 L. F. Nazar, M. Cuisinier and Q. Pang, *MRS Bull.*, 2014, **39**, 436–442.
32 N. Ding, L. Zhou, C. Zhou, D. Geng, J. Yang, S. W. Chien, Z. Liu, M.-F. Ng, A. Yu, T. S. A. Hor, M. B. Sullivan and Y. Zong, *Sci. Rep.*, 2016, **6**, 33154.
33 M. J. Lacey, A. Yalamanchili, J. Maibach, C. Tengstedt, K. Edström and D. Brandell, *RSC Adv.*, 2016, **6**, 3632–3641.
34 A. Rosenman, R. Elazari, G. Salitra, E. Markevich, D. Aurbach and A. Garsuch, *J. Electrochem. Soc.*, 2015, **162**, A470.
35 S. S. Zhang, *Electrochim. Acta*, 2012, **70**, 344–348.
36 S. Xiong, K. Xie, Y. Diao and X. Hong, *J. Power Sources*, 2014, **246**, 840–845.
37 D. Aurbach, E. Pollak, R. Elazari, G. Salitra, C. S. Kelley and J. Affinito, *J. Electrochem. Soc.*, 2009, **156**, A694.
38 M. T. Lee, H. Liu and D. Brandell, *Batteries Supercaps*, 2020, **3**, 1370–1376.
39 X. Liang, C. Hart, Q. Pang, A. Garsuch, T. Weiss and L. F. Nazar, *Nat. Commun.*, 2015, **6**, 5682.
40 X. Ye, J. Wu, J. Liang, Y. Sun, X. Ren, X. Ouyang, D. Wu, Y. Li, L. Zhang, J. Hu, Q. Zhang and J. Liu, *ACS Appl. Mater. Interfaces*, 2022, **14**, 53788–53797.
41 X.-Q. Zhang, X.-B. Cheng, X. Chen, C. Yan and Q. Zhang, *Adv. Funct. Mater.*, 2017, **27**, 1605989.
42 S. Choudhury and L. A. Archer, *Adv. Electron. Mater.*, 2016, **2**, 1500246.
43 G. Bieker, D. Diddens, M. Kolek, O. Borodin, M. Winter, P. Bieker and K. Jalkanen, *J. Phys. Chem. C*, 2018, **122**, 21770–21783.
44 Q. Zou and Y. C. Lu, *J. Phys. Chem. Lett.*, 2016, **7**, 1518–1525.
45 J. Häcker, D. H. Nguyen, T. Rommel, Z. Zhao-Karger, N. Wagner and K. A. Friedrich, *ACS Energy Lett.*, 2021, **7**, 1–9.
46 P. Han and A. Manthiram, *J. Power Sources*, 2017, **369**, 87–94.
47 Q. Zhang, Y. Wang, Z. W. Seh, Z. Fu, R. Zhang and Y. Cui, *Nano Lett.*, 2015, **15**, 3780–3786.
48 M. W. Hasan, K. Huynh, B. Lama, A. A. Razzaq, M. G. Smdani, F. N. Akter, B. Maddipudi, R. Shende, T. R. Paudel and W. Xing, *J. Electrochem. Soc.*, 2024, **171**, 040540.
49 R. L. Woodin and J. L. Beauchamp, *J. Am. Chem. Soc.*, 1978, **100**, 501–508.
50 I. Batatia, P. Benner, Y. Chiang, A. M. Elena, D. P. Kovács, J. Riebesell, X. R. Advincula, M. Asta, W. J. Baldwin and N. Bernstein, *arXiv*, 2023, preprint, arXiv:2401.00096, DOI: **10.48550/arXiv.2401.00096**.
51 I. Batatia, D. P. Kovacs, G. Simm, C. Ortner and G. Csányi, *Adv. Neural Inf. Process. Syst.*, 2022, **35**, 11423–11436.
52 J. C. Lytle, J. M. Wallace, M. B. Sassin, A. J. Barrow, J. W. Long, J. L. Dysart, C. H. Renninger, M. P. Saunders, N. L. Brandell and D. R. Rolison, *Energy Environ. Sci.*, 2011, **4**, 1913–1925.
53 R. Carter, L. Oakes, N. Muralidharan and C. L. Pint, *J. Phys. Chem. C*, 2017, **121**, 7718–7727.
54 M. Li, R. Carter, A. Douglas, L. Oakes and C. L. Pint, *ACS Nano*, 2017, **11**, 4877–4884.
55 R. Carter, B. Davis, L. Oakes, M. R. Maschmann and C. L. Pint, *Nanoscale*, 2017, **9**, 15018–15026.
56 G. Kresse and J. Furthmüller, *Phys. Rev. B: Condens. Matter Mater. Phys.*, 1996, **54**, 11169–11186.
57 P. E. Blöchl, *Phys. Rev. B: Condens. Matter Mater. Phys.*, 1994, **50**, 17953–17979.
58 J. Heyd, G. E. Scuseria and M. Ernzerhof, *J. Chem. Phys.*, 2003, **118**, 8207–8215.
59 S. Grimme, J. Antony, S. Ehrlich and H. Krieg, *J. Chem. Phys.*, 2010, **132**, 154104.